

Article

Control of the Optical Wavefront in Phase and Amplitude by a Single LC-SLM in a Stellar Coronagraph Aiming for Direct Exoplanet Imaging

Andrey Yudaev *, Alla Venkstern, Irina Shulgina, Alexander Kiselev, Alexander Tavrov and Oleg Korablev 

IKI RAS, Space Research Institute of Russian Academy of Sciences, 117997 Moscow, Russia

* Correspondence: yudaev@phystech.edu

Abstract: This article presents a novel approach to actively compensate wavefront errors in both phase and amplitude using a Liquid Crystal Spatial Light Modulator (LC-SLM) for direct exoplanet imaging. This method involves controlling the wavefront to address challenges posed by stellar coronagraphy. Experimental results demonstrate successful wavefront error compensation in both phase and amplitude components. This technique shows promise for direct exoplanet imaging and may be applied onboard orbital telescopes in the future.

Keywords: stellar coronagraphy; direct imaging; LC-SLM; rotational shear interferometer; wavefront sensing; wavefront control and correction; exoplanets

1. Introduction

In photonics, one of the most intriguing tasks is to visualize a point-like image of an Earth-type planet in the vicinity of a neighboring star (of Solar type) at a distance on the order of 10 parsecs. Formally, the spatial resolution of a meter class telescope in the optical wavelength range is sufficient by Rayleigh criterion to detect the outstanding peak of an exoplanet point spread function (PSF) at a *stellocentric* unnecessary distance of $1 \dots 10 \lambda/D$.

However, the luminosity ratio of star/planet is about $10^9 \dots 10^{10}$. The planet has insufficient contrast as the faint light source relative to the host star light source. We shall consider a two-meter class telescope because the effect of exozodi is surrounding and therefore masking a stellar vicinity [1,2]. If the telescope has an ideal optical quality and has a stellar coronagraph mounted after, such a coronagraph instrument can show a planet on an attenuated diffraction background of the host star or, more precisely, on the attenuated background of the stellar PSF wings.

Modern space optics offers diffraction-limited resolution; however, optics is not free from residual aberrations and micro-roughness, which result in a visible *halo* effect around the main maximum of the PSF. Certainly that masks the image of the faint planet light source. To move from a theoretical to a practical scope, one has to use precise adaptive optics (AO) in order to eliminate the wavefront (WF) error (WFE). The adaptive optics system aims to measure the WFE and then to compensate for it. One fundamentally analyses the diffraction problem resumes wavefront error in terms of complex amplitude [3]. One has to compensate not only for the phase component of the WFE, but also for its amplitude component.

The amplitude component of the WFE is caused by some zonal inhomogeneity in transmittance or/and reflection; as well, it is due to Fresnel diffraction on the micro-roughnesses, residual aberrations, and aperture boundaries of every optical element (or optical surface) mounted in the plane not being conjugated with the pupil of the optical system, e.g., a secondary telescope mirror, downstream coronagraph optics, a spider, apertures etc. Moreover, a fringe field effect can be caused in the LC layer that could distort the phase and amplitude wavefront profiles in outgoing light from the LC-SLM itself [4].



Citation: Yudaev, A.; Venkstern, A.; Shulgina, I.; Kiselev, A.; Tavrov, A.; Korablev, O. Control of the Optical Wavefront in Phase and Amplitude by a Single LC-SLM in a Stellar Coronagraph Aiming for Direct Exoplanet Imaging. *Photonics* **2024**, *11*, 300. <https://doi.org/10.3390/photonics11040300>

Received: 20 February 2024

Revised: 14 March 2024

Accepted: 21 March 2024

Published: 26 March 2024



Copyright: © 2024 by the authors. Licensee MDPI, Basel, Switzerland. This article is an open access article distributed under the terms and conditions of the Creative Commons Attribution (CC BY) license (<https://creativecommons.org/licenses/by/4.0/>).

A portrait of the Fresnel diffraction can be primitively illustrated via the Talbot effect for a periodic structure or via sharp boundary oscillating. To compensate for the WFE in the Fresnel zone (not in the Fraunhofer zone), we require an increasing number of controllable pixels or actuators if deformable mirrors (DM) are used.

In the present communication, we show new technique and demonstrate the start-up laboratory experiments aiming at the phase–amplitude correction for the WFE in a stellar interference coronagraph.

Omitting details, we shall address the reader to the published papers on the characteristics and operations of the stellar coronagraph, as constructed by a classical Lyot schematic with and without apodization schemes [5–7], and, in particular, by a coronagraph based on destructive interference process [8,9].

The working principle of an interfero coronagraph [10] is to superimpose with antiphase two pupil images being shifted [8], reversed, or rotated [11], or differently superposed [12]. The listed interferometers result in a destructive interference process. Therefore, an interferometer eliminates the starlight being received from the on-axis direction. Planetary (or companion) light does not interfere destructively because of the off-axis tilt (or shift or shear in a pupil). The image component from a planet becomes split into two copies; by superposition, they are spatially separated and do not interfere destructively. Interfero-coronagraphy is advantageous in terms of its broad spectral band achromaticity and, more generally, because of its small inner working angle (IWA). The IWA characteristic can be considered as the spatial resolution of a coronagraph instrument. The achromatic interfero-coronagraph (AIC) is known to have one of the smallest possible IWAs ($0.38 \lambda/D$), such as it was initially referred to in [10] with the fixed angle of a 180-deg. rotational shear. Later, it was redesigned into a modified Sagnac scheme, implementing the common path (or cyclic path or cavity) (CP-AIC) [13] aiming to relax the mechanic instability.

The severe functional disadvantage of an interfero coronagraph is known as the stellar leakage effect. Due to this effect, the starlight cannot be completely suppressed because the apparent size of the star is not physically infinitesimal [5]. The observed size of a star is far beyond the spatial resolution of a *single dish* optical telescope, but physically, the star size causes a non-fully coherent point-like source; considering spatial coherence, it causes an extended source. Numerous methods to reduce the stellar leakage effect, due to the infinitesimal apparent size of the star, have been proposed from the 180-deg. rotational shift to smaller angles [11] or to apply an apodization, e.g., a Sonine type [14].

In the present communication, the proposed method is applicable to the listed possible efforts to reduce the star leakage effect.

2. Method

Precise wavefront correction in phase and amplitude is ultimately required as pre-optics schematics for the coronagraph for its functionality. AO compensates for optical aberrations including optical defects given by the optical surfaces and apertures. Light radiation is collected by a telescope under or above the telluric atmosphere, and it is analyzed after a coronagraph by a field camera, spectroscopy, or different instrument. It is important to note that the measurement of the wavefront has to be organized after the coronagraph. Otherwise, a non-common-path wavefront error (NCP WFE) is caused by a different or incompletely similar optical path to the wavefront sensor (WFS). This generates additional phase and amplitude errors that become magnified [15] by the coronagraph.

Aiming active adaptive optics to control the WFE in phase and amplitude, we used a phase-only liquid crystal spatial light modulator (LC-SLM) mounted in a specific polarization schematic as shown in Figure 1 inside the dashed-line box I. In our work, we used the reflective type LC-SLM. In Figure 1, the LC-SLM is shown in transmittance mode for the purpose of simplification. It is better to mount the LC-SLM by an incident angle less than 15° to minimize depolarization effects, which can reduce the SLM modulation contrast [16]. In our setup the incident angle was about 4° .

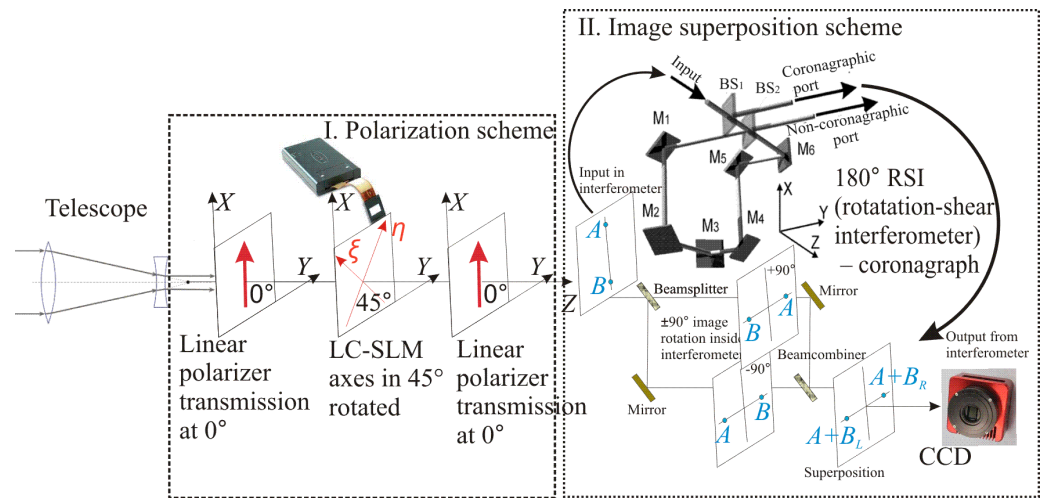


Figure 1. Optical schemes: I. Polarization scheme to orient LC-SLM (in dashed-line box) and II. Image superposition in rotation–shear interferometer (in dot-line box) simplified.

Math algebra of the polarization of Jones vectors and matrices was applied to describe the action of the *phase-only* LC-SLM being used as a phase and amplitude WFE corrector. We considered the output of the following polarization scheme: entrance linear polarization with the azimuth orientation at 45° to the X axis, LC-SLM with the phase modulation axis along X, and the final linear polarizer with transmission at 45° to X. See this set, in the dash-line box I in Figure 1.

Then, the phase–amplitude control of the WF is realized as:

$$\mathbf{E}_{out} = \mathbf{P}_{\beta=45^\circ} \mathbf{SLM} \mathbf{E}_{in} \tag{1a}$$

$$= \frac{1}{2} \begin{pmatrix} 1 & 1 \\ 1 & 1 \end{pmatrix} \begin{pmatrix} e^{i\alpha} & 0 \\ 0 & 1 \end{pmatrix} \frac{1}{\sqrt{2}} E e^{i\varphi} \begin{pmatrix} 1 \\ 1 \end{pmatrix} \tag{1b}$$

$$= \frac{1}{2\sqrt{2}} (e^{i\alpha} + 1) E e^{i\varphi} \begin{pmatrix} 1 \\ 1 \end{pmatrix}, \tag{1c}$$

$$= \tilde{E} e^{i\tilde{\varphi}_A} \begin{pmatrix} 1 \\ 1 \end{pmatrix} \tag{1d}$$

where $\mathbf{E}_{in} = E e^{i\varphi} \frac{1}{\sqrt{2}} \begin{pmatrix} 1 \\ 1 \end{pmatrix}$ defines an entrance wave, with the polarization linear state with a 45-deg. azimuth respective X axis, with the complex amplitude $E e^{i\varphi}$ at entrance, where E denotes the modulus (or amplitude) and φ —the phase. At the output of box I in Figure 1, the complex amplitude is denoted by $\tilde{E} e^{i\tilde{\varphi}_A}$.

$\mathbf{SLM} = \begin{pmatrix} e^{i\alpha} & 0 \\ 0 & 1 \end{pmatrix}$ defines the phase-only LC-SLM (liquid crystal spatial light modulator) with the phase angle modulation α along X, which is controlled by an externally applied electric voltage.

$\mathbf{P}_{\beta=45^\circ} = \frac{1}{2} \begin{pmatrix} 1 & 1 \\ 1 & 1 \end{pmatrix}$ defines the linear polarizer oriented by its transmission axis at 45-deg. to the X axis.

From Equation (1c), it can be seen that the control of α leads to a change not only in the phase but also in the amplitude of the complex field. This useful property is next applied to a phase–amplitude correction of the wavefront.

Presented here, a phase–amplitude correction of the WFE is entirely developed for the optical schemes, which use the principle of a nulling interferometer with rotational shift functioning as a stellar coronagraph [11,13]. A shear interferometer has two mutually shifted waves being superposed. This allows two degrees of freedom: two controls (modu-

lations) α_A and α_B , at two “coupled” points “A” and “B” of the initial wavefront, which are superimposed. We aim these controls to obtain the mostly accurate “dark field” destructive interference condition.

Let us consider that the shear interferometer superposes two electric fields E_{out_A} and E_{out_B} in points “A” and “B”. This is illustrated in Figure 1; see the dot-line box II. Before the interferometer, at the initially separated WF symmetric points “A” and “B”, by the SLM we control the complex amplitudes $E_{out_A}(\alpha_A) = \tilde{E}_A e^{i\tilde{\varphi}_A}$ and $E_{out_B}(\alpha_B) = \tilde{E}_B e^{i\tilde{\varphi}_B}$; see Equation (1d). The destructive interference regime requires both the following conditions (i) and (ii).

(i): A zero-phase difference before the interferometer while we count on an additional phase shift of π implemented inside the nulling interferometer [11,13]:

$$\Delta\varphi = \tilde{\varphi}_A - \tilde{\varphi}_B \rightarrow 0. \tag{2a}$$

(ii): The equality of the moduli of the complex amplitudes:

$$\frac{\tilde{E}_A}{\tilde{E}_B} \rightarrow 1. \tag{2b}$$

Therefore, to satisfy both the phase (2a) and amplitude (2b) conditions, we have to consider the electric fields in two *coupled* (by following superposition) points A and B in a pupil before 180° RSI. Their waves interfere further in the conjugated pupil plane at the dark port (with implemented anti-phase) of the interferometer at the point denoted as A + B (See Figure 1, dot-line box II).

Now, we recall the polarization scheme in Figure 1, in dashed-line box I. Then the complex amplitudes of the electric field at points A and B with respective α_A and α_B modulations via the LC-SLM control are defined according to (1a)–(1d):

$$E_{out_A}(\alpha_A) = \frac{1}{2\sqrt{2}} (e^{i\alpha_A} + 1) E_A e^{i\varphi_A} \begin{pmatrix} 1 \\ 1 \end{pmatrix} = \tilde{E}_A e^{i\tilde{\varphi}_A}, \tag{3a}$$

$$E_{out_B}(\alpha_B) = \frac{1}{2\sqrt{2}} (e^{i\alpha_B} + 1) E_B e^{i\varphi_B} \begin{pmatrix} 1 \\ 1 \end{pmatrix} = \tilde{E}_B e^{i\tilde{\varphi}_B}, \tag{3b}$$

We stress here, again, our notations for the complex amplitudes moduli: E_A, E_B and phases φ_A, φ_B (without *tilde*) which describe the initial wavefront (before the LC-SLM), while the complex amplitudes moduli \tilde{E}_A, \tilde{E}_B and the phases $\tilde{\varphi}_A, \tilde{\varphi}_B$ (with *tilde*) denote the corresponding values after the LC-SLM and polarizer (after the polarization scheme $\mathbf{P}_{\beta=45^\circ}$ SLM \mathbf{E}_{in} ; see Equation (1a)).

After passing the interferometer, on its dark port, by coherent wave subtraction, we have the complex field amplitude at point A + B by the superposition of waves $\mathbf{E}_{out_A}, \mathbf{E}_{out_B}$:

$$\mathbf{E}_{A+B} = \mathbf{E}_{out_A} + \mathbf{E}_{out_B} \tag{4a}$$

$$= \frac{E_A}{2\sqrt{2}} (e^{i\alpha_A} + 1) e^{i\varphi_A} + \frac{E_B}{2\sqrt{2}} (e^{i\alpha_B} + 1) e^{i(\varphi_B+\pi)}. \tag{4b}$$

The CCD detects the intensity I_{A+B} of the interference pattern, e.g., in the A + B point after ensemble averaging (where $\langle \dots \rangle$ defines the ensemble average over an exposure time):

$$I_{A+B} = \langle E_{A+B} \overline{E_{A+B}} \rangle = \mathbf{E}_{out_A}^2 + \mathbf{E}_{out_B}^2 + \mathbf{E}_{out_A} \overline{\mathbf{E}_{out_B}} + \mathbf{E}_{out_B} \overline{\mathbf{E}_{out_A}}, \tag{5}$$

where the *upper underline* denotes the complex conjugate (in matrix form it denotes the Hermitian conjugate).

Substituting (4) into (5), we can express the detected intensity I_{A+B} through the complex amplitude moduli (E_A, E_B) and the phase difference $\Delta_\varphi = \varphi_A - \varphi_B$ of the electric fields in the entrance pupil WF and the corresponding SLM modulations (α_A, α_B):

$$I_{A+B} = I(E_A, E_B, \Delta_\varphi; \alpha_A, \alpha_B) \tag{6a}$$

$$= E_A^2 + E_B^2 + E_A^2 \cos(\alpha_A) + E_B^2 \cos(\alpha_B) - E_A E_B (\cos(\Delta_\varphi) + \cos(\alpha_A + \Delta_\varphi) + \cos(\alpha_B - \Delta_\varphi) + \cos(\alpha_A - \alpha_B + \Delta_\varphi)). \tag{6b}$$

2.1. Measurement of the Wavefront

For the sake of brevity, we show here the algorithm of the wavefront measurement to determine amplitude and phase difference $E_A, E_B; \Delta_\varphi$ by I_{A+B} intensity measurements, which is their function, (6a). We study Equations in (6): if one measures a series ($j = (1..3)$) of three intensities $I_{A+B}^j = I_j(E_A, E_B, \Delta_\varphi; \alpha_A^j, \alpha_B^j)$ in the plane conjugated to the pupil (the SLM is set in the pupil) by providing certain SLM modulations as parameters α_A^j and α_B^j in the *coupled* points A and B , he determines the phase difference Δ_φ and the amplitudes E_A and E_B for the next step of WFE correction.

For example, a three-step $j = (1..3)$ procedure to determine Δ_φ, a_A, a_B detects three intensities by SLM modulations set as $\{\alpha_A, \alpha_B\} = \{ (0, 0), (\pi, 0), (0, \pi) \}$:

$$\begin{cases} I_1(E_A, E_B, \Delta_\varphi; 0, 0) = I(0, 0), \\ I_2(E_A, E_B, \Delta_\varphi; \pi, 0) = I(\pi, 0), \\ I_3(E_A, E_B, \Delta_\varphi; 0, \pi) = I(0, \pi). \end{cases} \tag{7}$$

Entrance wavefront characteristics Δ_φ, E_A, E_B we determine from solving the system of Equation (7) by their expression as (6b):

$$E_A = \sqrt{\frac{I(0, \pi)}{2}}, \tag{8a}$$

$$E_B = \sqrt{\frac{I(\pi, 0)}{2}}, \tag{8b}$$

$$\Delta_\varphi = \arccos\left(\frac{I(0, 0) - 4E_A^2 - 4E_B^2}{8E_A E_B}\right). \tag{8c}$$

Certainly, the wavefront measurement method can be modified and improved in accuracy, e.g., by increasing the number j of measurements $I_{A+B}^j = I_j(E_A, E_B, \Delta_\varphi; \alpha_A^j, \alpha_B^j)$, similar to phase shifting interferometry [17].

We resume here that by means of Equations (8a)–(8c), it is possible to measure the wavefront error in terms E_A, E_B, Δ_φ at symmetric (or coupled by electric fields superposition) points A and B . Therefore, we can restore the spatial distribution of WFE pixel wise.

2.2. Wavefront Correction by Phase-Amplitude Modulation

We intend to show here a method to correct the wavefront error, taking into account three measured wavefront characteristics: E_A, E_B, Δ_φ . These measured WFE characteristics at the coupled pupil points A and B are associated with subsequent interference in the $A + B$ point. This correction method is easily extended to cover all the pupil points.

2.2.1. Phase Correction

To present the WFE correction problem, at first, we simplify considering the phase-only WFE: $\Delta_\varphi \neq 0, \Delta_E = (E_A - E_B) = 0$.

Figure 2 depicts schematically the principle of phase correction in the *coupled* points A and B . Here, the φ_A and φ_B denote the phases in the *coupled* points A and B (set diametrically opposite) in the pupil plane where the SLM is installed. After passing through the RSI interferometer, an optically conjugated pupil plane is formed. Here, in the points denoted

$A + B, L$ (in the left half-plane) and $A + B, R$ (in the right half-plane), the interference signals intensities of interference pattern $I_{A+B, L}, I_{A+B, R}$ become proportional to the cosine of $\Delta\varphi = \varphi_A - \varphi_B$:

$$I_{A+B, R} \sim \cos(-\Delta\varphi), \tag{9a}$$

$$I_{A+B, L} \sim \cos(\Delta\varphi). \tag{9b}$$

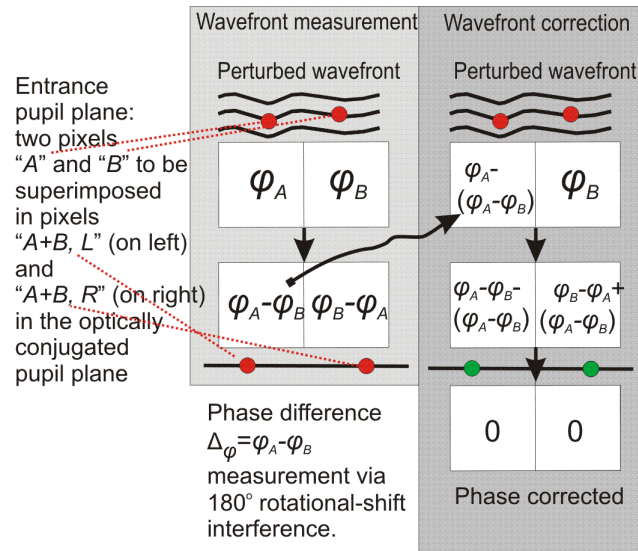


Figure 2. Algorithm to measure (see left column) and to correct (see left column) a phase-only wavefront error (WFE) in 180-deg. rotational-shift interferometer (interfero coronagraph).

Because the cosine function is even visually through the recorded intensity, there is no difference between the left and right half-planes: $I_{A+B, R} = I_{A+B, L}$, but physically, the relationship (9) turns out to be important to organize the proper wavefront correction.

The measured phase difference $\Delta\varphi$ is added then as an additional phase shift to the phase of point A (on the left) or to the right point B (but with a negative sign of $\Delta\varphi$ not shown in the figure). In Figure 2, next after passing through the interferometer RSI, at the two points $A + B, L$ and $A + B, R$ (shown in green), the corrected phase difference becomes $\tilde{\Delta\varphi} \equiv 0$, which means the phase-only aberrations (or wavefront errors) have been successfully corrected.

2.2.2. Phase- and Amplitude Wavefront Error Correction

We analyze here the algorithm to correct a more complex WFE by $\Delta\varphi \neq 0$ (in phase), $\Delta E = E_A - E_B \neq 0$ (and in amplitude), which in contrast to the phase-only correction (discussed above in Section 2.2.1), contains an additional amplitude imbalance correction option.

For simplicity, we denote $I_{A+B} = I_{A+B, R} = I_{A+B, L}$, see Equation (9a,9b). According to Equations (4) and (5), we search for such modulations α_A and α_B that cause a zero-intensity at this point: $I_{A+B} = \langle \mathbf{E}_{A+B} \overline{\mathbf{E}_{A+B}} \rangle \rightarrow 0$. We solve therefore the following equation:

$$\frac{E_A}{E_B} (e^{i\alpha_A} + 1) e^{i\varphi_A} = (e^{i\alpha_B} + 1) e^{i(\varphi_B)}, \tag{10}$$

aiming to find two unknowns, α_A and α_B , each of which depends on four variables: the moduli of complex amplitudes of fields E_A, E_B , and the phases φ_A, φ_B . We reduce four variables to two variables, which are physically relevant in the frame of our model, namely the amplitude ratio: $k = \frac{E_A}{E_B}$ and the phase difference: $\Delta\varphi = \varphi_A - \varphi_B$. The k and $\Delta\varphi$ are real numbers, and they were measured by Equations (8a)–(8c). Equation (10) has the following solution:

$$\alpha_A = \tan^{-1} \left(\frac{-1 + 2 \frac{E_A}{E_B} \cos \Delta\varphi - \left(\frac{E_A}{E_B} \cos \Delta\varphi \right)^2 + \left(\frac{E_A}{E_B} \sin \Delta\varphi \right)^2}{2 \frac{E_A}{E_B} \left(-1 + \frac{E_A}{E_B} \cos \Delta\varphi \right) \sin \Delta\varphi} \right), \quad (11a)$$

$$\alpha_B = \tan^{-1} \left(\frac{\left(\frac{E_A}{E_B} \right)^2 - 2 \frac{E_A}{E_B} \cos \Delta\varphi + \cos 2\Delta\varphi}{-2 \left(\cos \Delta\varphi - \frac{E_A}{E_B} \right) \sin \Delta\varphi} \right). \quad (11b)$$

We did not simplify the arctangent arguments in $\alpha_A \left(\frac{E_A}{E_B}, \Delta\varphi \right)$, Equation (11a), and in $\alpha_B \left(\frac{E_A}{E_B}, \Delta\varphi \right)$, Equation (11b), and we left them in ratios to use the function $\tan^{-1} \left(\frac{Y}{X} \right) = \arctan2(X, Y)$ [18].

3. Simulation

Figure 3 illustrates some numerical verifications to validate the analytical solution found by Equation (11). In the figure, an analytical solution via Equation (11) is shown by the red cross unnecessary mark and coincides visually with the minimum in intensity in the logarithmic scale $\log_{10}(I_{A+B}(\alpha_A, \alpha_B))$ of the interference pattern shown by the background colormap. The latter was evaluated by a trivial enumeration of α_A, α_B in the mesh region $\alpha_A, \alpha_B \in [-\pi, \pi]$ by the values $k = \frac{E_A}{E_B} = 1.11$; $\Delta\varphi = -0.1$ radians, where the used k and $\Delta\varphi$ have been chosen arbitrarily. The red cross mark position in $\{\alpha_A, \alpha_B\}$ coordinates mesh assigns the global minimum.

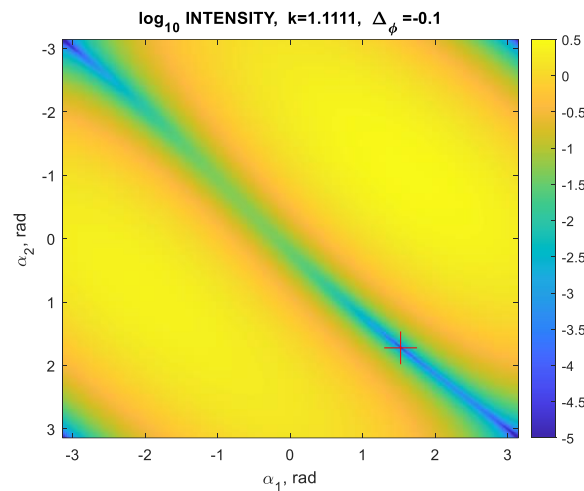


Figure 3. Check for an analytical solution Equation (11). In title are shown initial amplitude imbalance k and phase difference $\Delta\varphi$.

In Figure 4, we analyze an intensity transmission characteristic $T(\alpha_A, \alpha_B)$, which shows the attenuation of the signal (from a faint exoplanet) in a single pupil pixel because we corrected the amplitude imbalance of $k = 1.11$. In a pixel, the planetary intensity signal transmission $T(\alpha_A, \alpha_B) \approx 0.65$ becomes reduced relative to unitary because an amplitude correction attenuates the transmission of both signals from the star and planet. We have considered here the WFE in point $A + B$ by $k = \frac{E_A}{E_B} = 1.11$; $\Delta\varphi = -0.1$. The Figure 4 background has the colormap that is the two-dimensional distribution of $T(\alpha_A, \alpha_B)$ being evaluated in the domain of $\alpha_A, \alpha_B \in [-\pi, \pi]$.

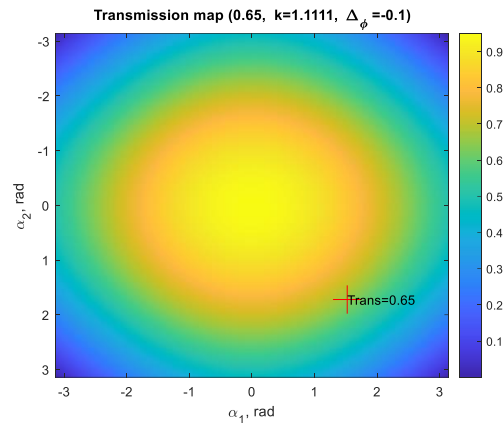


Figure 4. Transmission characteristic $T(\alpha_A, \alpha_B)$ can be associated with the planetary signal intensity $i.3n$ a single pixel.

In Figure 5, in a $\pm 15 \lambda/D$ focal image domain we show several simulation graphs to compare the images (1) in non-coronagraphic mode, (2) in coronagraphic mode without any WFE correction, (3) in coronagraphic mode with WFE phase-only correction, and (4) in coronagraphic mode with WFE phase and amplitude correction. These images are resumed by azimuth-averaged stellocentric cross-sections (5).

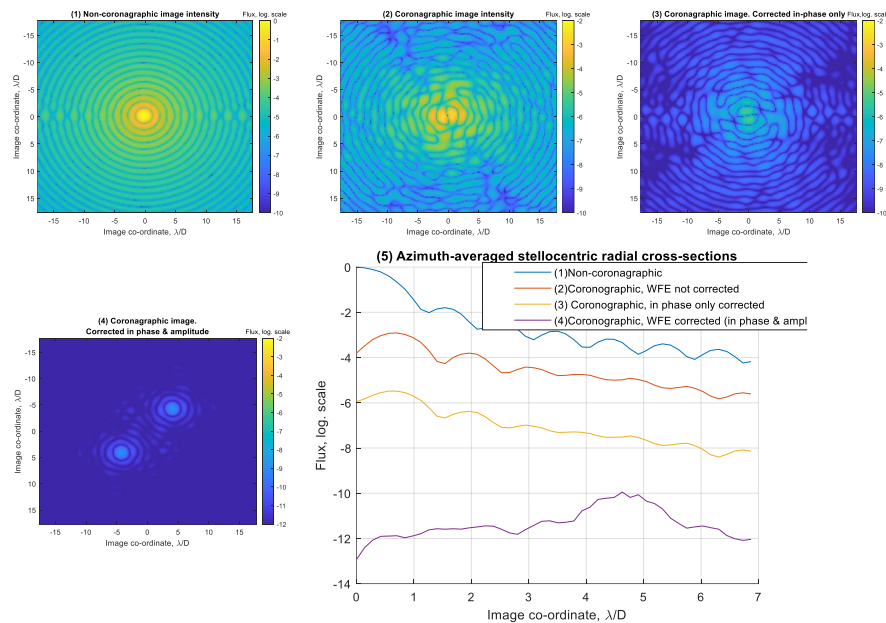


Figure 5. Non-coronagraphic (1) and coronagraphic images (2)–(4) simulated by phase error $\lambda/50$ rms and the amplitude error 5%; (3) phase-only corrected image; (4) phase and amplitude corrected image resolves a planet companion; (5) azimuth-averaged radial stellocentric profiles corresponding (1)–(4) shows gradual scattered stellar background suppression.

In simulations in Figure 5, one can see that, caused by diffraction and scattering on residual aberrations and surface micro-roughness, the stellar background shows the gradual suppression by means of the coronagraph without and with the wavefront control. The wavefront control was performed by correcting the phase-only wavefront errors at first, then correcting both the phase and amplitude WFE. In these simulations, the parameters were phase deviations of about $\lambda/50$ rms at $\lambda = 600$ nm and amplitude deviations of about 5%.

4. Laboratory Experiment

In the laboratory experiment, we studied the above proposed approach to correct the complex value wavefront error simultaneously in phase and amplitude at the wavelength 632.8 nm. In addition to our previously published efforts [9] where we performed the phase-only wavefront control, here, we succeeded in both measuring the complex number WFE, and then controlling the WFE in phase and amplitude operating by a spatial light modulator (SLM) being inserted in the optical and polarization scheme, as in Figure 1. We used a commercially available LC-SLM from HOLOEYE© (Berlin, Germany): model PLUTO-2.1-VIS-016. It has an 8 μm pixel size with a resolution up to 1920 × 1080 active pixels and a response time of ~66 ms [19]. The LC-SLM was capable of providing a maximum phase shift of about 5.2 π (on the working wavelength 630 nm), but it was calibrated to provide only reduced 2π of maximum phase shift, that was sufficient for the described correction method. The camera used in the setup was a CMOS monochrome camera from Edmund Optics© (Barrington, NJ, USA), model EO-5012M with a pixel size of 2.2 μm and a resolution of up to 2056 × 1920. It was synced with the LC-SLM by a dedicated frame sync signal. Several experimental results are shown in Figure 6, where we demonstrate the gradually reducing azimuth-averaged cross-sections of the non-coronagraphic PSF, the coronagraphic PSF without WFE correction, and the coronagraphic PSF with WFE correction in phase and amplitude; see panel (a). In Figure 6 in panels (b) and (c), we show noncorrected fragments of pupil intensities after the coronagraph, where the WFE was noncorrected and corrected. Corresponding histograms are shown in panels (d) and (e). If one analyzes pupil fragments (b) and (c), he finds at first the decreased intensity level; see the colorbar scale on the left. Integrally, this decrease corresponds in numbers to the ratio of the coronagraphic PSF without applied WFE correction (shown in the azimuth-averaged section by the red color graph in panel (a)) to the coronagraphic PSF with WFE correction (shown by the orange color graph). Additionally, the corresponding histogram (in panels (d) and (e)) demonstrate that the intensity deviations decrease after correction. Because of amplitude attenuation, we estimated the virtual planetary signal had its throughput at about 0.92 as averaged over all pixels.

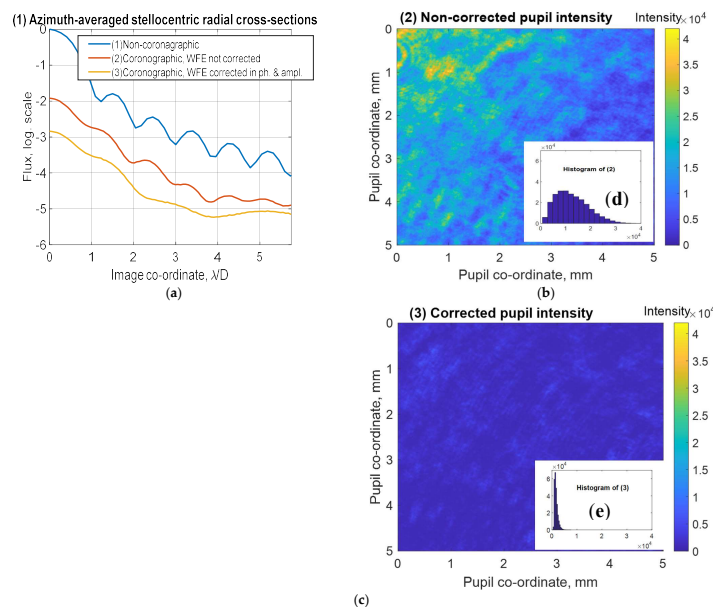


Figure 6. Experimental data of wavefront error correction in phase and amplitude regime. (a) Azimuth-averaged PSF cross-sections: blue (1) line—non-coronagraphic PSF; red (2) line—coronagraphic PSF without WFE correction; orange (3) line—coronagraphic PSF with WFE correction. (b,c) Coronagraphic pupil, the same areas before and after correction with corresponding histograms in panels (d,e).

5. Discussion

In the present article, we have continued the studies of our previous communication [9], where we just roughly sketched some general possibilities about how to correct wavefronts, not only in phase but simultaneously in amplitude. This is realized by the LC-SLM providing general polarization modulation at first, then it is converted in phase and in amplitude wavefront components by the linear polarizer mounted after the LC-SLM. Therefore, in the present communication, we have aimed to find and to test a practical analytical solution for wavefront error active correction both in phase and amplitude. This is shown analytically as well by numerical simulation and in a simple experiment in an optical lab.

Here, our goal was not to reach a high coronagraphic contrast in stellar light suppression, but we studied an appropriate optical architecture to control WFE. At first, we measured both the WFE phase and amplitude components. Then we operated by controlling voltages at an adaptive optics unit (LC-SLM) to correct wavefront error simultaneously in phase and amplitude. The advantages are the following: (i) both the wavefront measurement and the correction have been realized without any mechanical motion in the optical scheme and without its reconfiguration; (ii) such a WFE measurement was performed after the coronagraph, therefore we excluded possible non-common-path aberrations (NCPAs).

The simple approach presented here was found analytically and it was tested numerically by simulations using the Proper [20]. Finally, we designed an optical experiment in the lab, which has demonstrated the right tendency in deeper signal suppression in coronagraphic mode for an on-axis light source (that imitated starlight) by wavefront correction.

In future, we are optimistic about applying this technique onboard of an orbital telescope for direct exoplanet imaging. LC-SLM technology was *scientifically* tested under a thermo-vacuum environment [21], however not yet under the space requirement. A possible LC-SLM mounting can be in a chamber with an optical window, with stabilized normal temperature and pressure. Radiation tests are not known, but a telescope can be launched in a low orbit beneath the Van Allen radiation belt. Active adaptive optics competes with the static correction, but in space, an orbital telescope is stabilized statically up to certain level. Solar radiation plus heat generation by electronics causes a low speed mechanical instability of the primary mirror geometry and to optics having requirements greater than $\lambda/100$ in optical wavelength domain. Therefore, precise adaptive optics with the functions of measurement and the control of the wavefront in phase and simultaneously in amplitude remains advanced.

Author Contributions: Conceptualization, methodology, A.T. and A.Y.; part of math., A.V.; software, A.Y. and I.S.; experiment, A.T., A.Y. and A.K.; writing—original draft preparation, A.Y.; supervision, A.T. and O.K. All authors have read and agreed to the published version of the manuscript.

Funding: This research received no external funding.

Institutional Review Board Statement: Not applicable.

Informed Consent Statement: Not applicable.

Data Availability Statement: The data presented in this study are available on request from the corresponding author.

Conflicts of Interest: The authors declare no conflict of interest.

References

1. Traub, W.; Oppenheimer, B. Direct imaging of exoplanets. In *Exoplanets*; Seager, S., Ed.; University of Arizona Press: Tucson, AZ, USA, 2011; pp. 111–156. Available online: <https://www.amnh.org/content/download/53052/796511/file/DirectImagingChapter.pdf> (accessed on 16 January 2024).
2. Collisional Exozodi Simulation Catalog. Available online: <https://asd.gsfc.nasa.gov/Christopher.Stark/catalog.php> (accessed on 16 January 2024).
3. Goodman, J.W. *Introduction to Fourier Optics*, 3rd ed.; Roberts & Co. Publishers: Englewood, CO, USA, 2005; 491p.
4. Huang, Y.; Liao, E.; Chen, R.; Wu, S.-T. Liquid-Crystal-on-Silicon for Augmented Reality Displays. *Appl. Sci.* **2018**, *8*, 2366. [CrossRef]

5. Guyon, O.; Pluzhnik, E.A.; Kuchner, M.J.; Collins, B.; Ridgway, S.T. Theoretical Limits on Extrasolar Terrestrial Planet Detection with Coronagraphs. *Astrophys. J. Suppl. Ser.* **2006**, *167*, 81–99. [[CrossRef](#)]
6. Guyon, O. Extreme Adaptive Optics. *Annu. Rev. Astron. Astrophys.* **2018**, *56*, 315–355. [[CrossRef](#)]
7. Galicher, R.; Mazoyer, J. Imaging exoplanets with coronagraphic instruments. *Comptes Rendus Phys.* **2023**, *24*, 1–45. [[CrossRef](#)]
8. Lyon, R.; Clampin, M.; Woodruff, R.; Vasudevan, G.; Shao, M.; Levine, M.; Ge, J. Visible Nulling Coronagraphy for Exo-Planetary Detection and Characterization. *Proc. Int. Astron. Union* **2005**, *1*, 345–352. [[CrossRef](#)]
9. Yudaev, A.; Kiselev, A.; Shashkova, I.; Tavrov, A.; Lipatov, A.; Korablev, O. Wavefront Sensing by a Common-Path Interferometer for Wavefront Correction in Phase and Amplitude by a Liquid Crystal Spatial Light Modulator Aiming the Exoplanet Direct Imaging. *Photonics* **2023**, *10*, 320. [[CrossRef](#)]
10. Baudoz, P.; Rabbia, Y.; Gay, J. Achromatic interfero coronagraphy. *Astron. Astrophys. Suppl. Ser.* **2000**, *141*, 319–329. [[CrossRef](#)]
11. Frolov, P.; Shashkova, I.; Bezymyannikova, Y.; Kiselev, A.; Tavrov, A. Achromatic interfero-coronagraph with variable rotational shear: Reducing of star leakage effect, white light nulling with lab prototype. *J. Astron. Telesc. Instrum. Syst.* **2015**, *2*, 011002. [[CrossRef](#)]
12. Lyon, R.G.; Hicks, B.A.; Clampin, M.; Petrone, P.R., III. Phase-Occultation Nulling Coronagraphy. *arXiv* **2015**. [[CrossRef](#)]
13. Tavrov, A.V.; Kobayashi, Y.; Tanaka, Y.; Shioda, T.; Otani, Y.; Kurokawa, T.; Takeda, M. Common-path achromatic interferometer-coronagraph: Nulling of polychromatic light. *Opt. Lett.* **2005**, *30*, 2224–2226. [[CrossRef](#)] [[PubMed](#)]
14. Aime, C.; Rabbia, Y.; Carlotti, A.; Ricort, G. Reducing star leakage with a nuller coronagraph. An analytic approach for a Sonine apodized circular aperture. *A&A* **2011**, *530*, A52. [[CrossRef](#)]
15. Nishikawa, J.; Murakami, N. Unbalanced nulling interferometer and precise wavefront control. *Opt. Rev.* **2013**, *20*, 453–462. [[CrossRef](#)]
16. Chen, H.-M.P.; Yang, J.-P.; Yen, H.-T.; Hsu, Z.-N.; Huang, Y.; Wu, S.-T. Pursuing High Quality Phase-Only Liquid Crystal on Silicon (LCoS) Devices. *Appl. Sci.* **2018**, *8*, 2323. [[CrossRef](#)]
17. Malacara, D. *Optical Shop Testing*, 3rd ed.; John Wiley & Sons, Inc.: Hoboken, NJ, USA, 2006; ISBN 9780471484042.
18. Available online: <https://en.wikipedia.org/wiki/Atan2> (accessed on 16 January 2024).
19. HOLOEYE. Spatial Light Modulators. Available online: <https://holoeye.com/spatial-light-modulators> (accessed on 16 January 2024).
20. PROPER. Optical Propagation Library. Available online: <https://proper-library.sourceforge.net> (accessed on 16 January 2024).
21. Manuel, S.-L.; Antonio, C.-J.; Alberto, Á.-H. Validation of a spatial light modulator for space applications. In Proceedings of the SPIE 11180, International Conference on Space Optics—ICSO 2018, 111806R, Chania, Greece, 12 July 2018. [[CrossRef](#)]

Disclaimer/Publisher’s Note: The statements, opinions and data contained in all publications are solely those of the individual author(s) and contributor(s) and not of MDPI and/or the editor(s). MDPI and/or the editor(s) disclaim responsibility for any injury to people or property resulting from any ideas, methods, instructions or products referred to in the content.